

## Spin-Delocalization in Charged States of *para*-Phenylene-Linked Dendritic Oligoarylamines<sup>†</sup>

Akihiro Ito,\* Daisuke Sakamaki, Yusuke Ichikawa, and Kazuyoshi Tanaka

Department of Molecular Engineering, Graduate School of Engineering, Kyoto University, Nishikyō-ku, Kyoto 615–8510, Japan

Received August 1, 2010. Revised Manuscript Received November 22, 2010

Two kinds of basic dendritic (or starburst) all-*para*-phenylene-linked oligotriarylamines, which are generated from *para*-phenylenediamine and triphenylamine as core units, respectively, were prepared, and the electrochemical, spectroelectrochemical, ESR spectroscopic measurements were carried out with respect to their application as hole transport materials in optoelectronic devices such as organic light-emitting devices. The prepared dendritic oligoarylamines exhibits the multiredox-active properties, and are stably oxidizable up to tetra- or hexacations. According to the degree of oxidation, it was suggested that the charge distribution of the charged states gradually change so as to reduce the electrostatic repulsion between increased charges on the basis of the spectroelectrochemical studies. Moreover, the stability of the generated radical cations and the spin distribution in their radical cations were confirmed by the ESR measurements.

### Introduction

Since the first report of the multilayered organic light-emitting diodes (OLEDs) made from a bistriaryamine and Alq<sub>3</sub> by Tang and VanSlyke,<sup>1</sup> triaryamine derivatives have become one of the main components in OLED devices.<sup>2</sup> Because of their electron-rich property, the positively charged (or hole) states of aromatic amines are generally so stable that they act as good hole-transport materials in various applications such as xerography, solar cells, photorefractive systems, and so forth, in addition to the use of hole-transport layer for OLED devices.<sup>2</sup> Hence, the efforts in the synthesis of many kinds of oligotriarylamines and their polymers are being continued to clarify their characterization in device performance. In particular, “star-shaped” oligoarylamines are considered to be useful for the wide variety of electro-optical applications because of their ability to form grassy amorphous phases.<sup>2</sup> In addition, the intervalence (IV) compounds bearing two redox-active amino groups have been exhaustively examined so far, and it has been clarified

that the *para*-phenylene-linked bistriarylamines have the delocalized and/or almost delocalized IV states.<sup>3–6</sup>

In this study, we focused on two kinds of dendritic (or starburst) all-*para*-phenylene-linked oligotriarylamines **1** and **2**, which are generated from *para*-phenylenediamine and triphenylamine as core units, respectively (Chart 1). Although the dendritic compound possessing the same<sup>7</sup> and/or similar<sup>8–12</sup> molecular backbone as **2** has been

<sup>†</sup> Accepted as part of the “Special Issue on  $\pi$ -Functional Materials”.

\*Corresponding author. E-mail: aito@scl.kyoto-u.ac.jp.

(1) Tang, C. W.; Van Slyke, S. A. *Appl. Phys. Lett.* **1987**, *51*, 913.

(2) (a) Shirota, Y. *J. Mater. Chem.* **2000**, *10*, 1. (b) Thelakkat, M. *Macromol. Mater. Eng.* **2002**, *287*, 442. (c) Shirota, Y.; Kageyama, H. *Chem. Rev.* **2007**, *107*, 953.

(3) (a) Nelsen, S. F.; Tran, H. Q.; Nagy, M. A. *J. Am. Chem. Soc.* **1998**, *120*, 298. (b) Nelsen, S. F.; Ismagilov, R. F.; Powell, D. R. *J. Am. Chem. Soc.* **1998**, *120*, 1924. (c) Nelsen, S. F.; Ismagilov, R. F.; Teki, Y. *J. Am. Chem. Soc.* **1998**, *120*, 2200. (d) Bailey, S. E.; Zink, J. I.; Nelsen, S. F. *J. Am. Chem. Soc.* **2003**, *125*, 5939. (e) Lockard, J. V.; Zink, J. I.; Konradsson, A. E.; Weaver, M. N.; Nelsen, S. F. *J. Am. Chem. Soc.* **2003**, *125*, 13471.

(4) (a) Lambert, C.; Nöll, G. *J. Am. Chem. Soc.* **1999**, *121*, 8434. (b) Szeghalmi, A. V.; Erdmann, M.; Engel, V.; Schmitt, M.; Amthor, S.; Kriegisch, V.; Nöll, G.; Stahl, R.; Lambert, C.; Leusser, D.; Stalke, D.; Zabel, M.; Popp, J. *J. Am. Chem. Soc.* **2004**, *126*, 7834.

(5) (a) Coropceanu, V.; Lambert, C.; Nöll, G.; Brédas, J.-L. *Chem. Phys. Lett.* **2003**, *373*, 153. (b) Coropceanu, V.; Gruhn, N. E.; Barlow, S.; Lambert, C.; Durivage, J. C.; Bill, T. G.; Nöll, G.; Marder, S. R.; Brédas, J.-L. *J. Am. Chem. Soc.* **2004**, *126*, 2727.

(6) Nishiumi, T.; Nomura, Y.; Chimoto, Y.; Higuchi, M.; Yamamoto, K. *J. Phys. Chem. B* **2004**, *108*, 7992.

(7) (a) Louie, J.; Hartwig, J. F. *J. Am. Chem. Soc.* **1997**, *119*, 11695. (b) Ranasinghe, M. I.; Varnavski, O. P.; Pawlas, J.; Hauck, S. I.; Louie, J.; Hartwig, J. F.; Goodson, T. *J. Am. Chem. Soc.* **2002**, *124*, 6520.

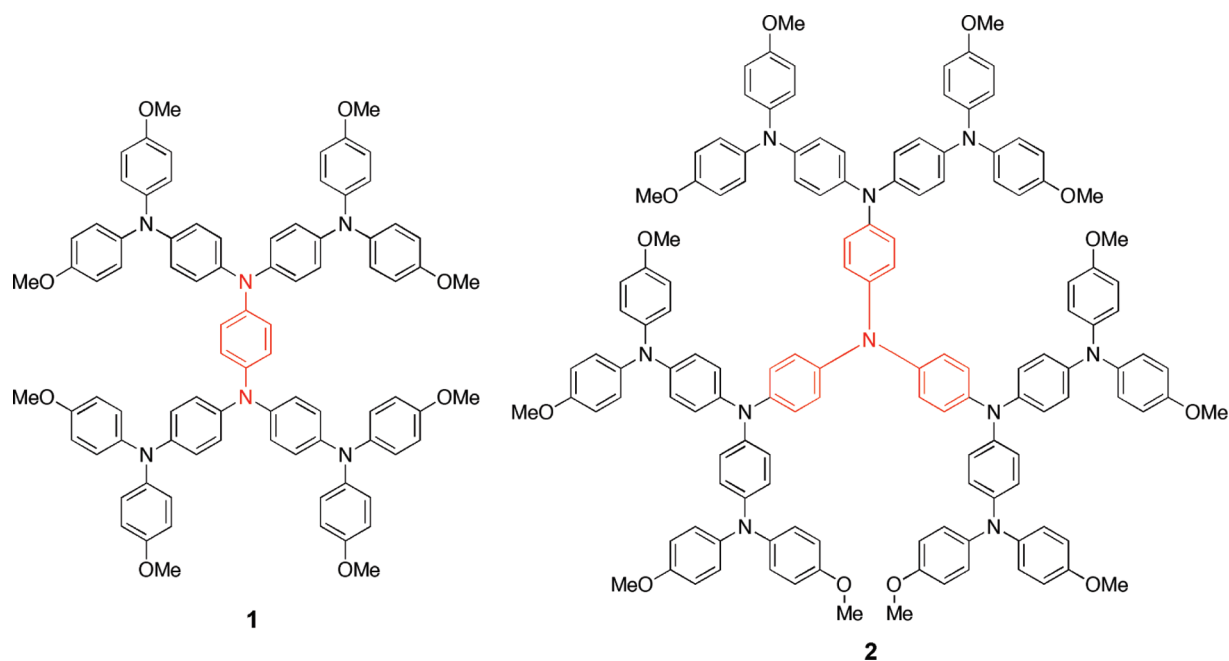
(8) Hagedorn, K. V.; Varnavski, O.; Hartwig, J.; Goodson, T. *J. Phys. Chem. C* **2008**, *112*, 2235.

(9) (a) Yoshizawa, K.; Chano, A.; Ito, A.; Tanaka, K.; Yamabe, T.; Fujita, H.; Yamauchi, J.; Shiro, M. *J. Am. Chem. Soc.* **1992**, *114*, 5994. (b) Ito, A.; Ino, H.; Matsui, Y.; Hirao, Y.; Tanaka, K.; Kanemoto, K.; Kato, T. *J. Phys. Chem. A* **2004**, *108*, 5715. (c) Hirao, Y.; Ino, H.; Ito, A.; Tanaka, K.; Kato, T. *J. Phys. Chem. A* **2006**, *110*, 4866. (d) Hirao, Y.; Ishizaki, H.; Ito, A.; Kato, T.; Tanaka, K. *Eur. J. Org. Chem.* **2007**, 186. (e) Hirao, Y.; Ito, A.; Tanaka, K. *J. Phys. Chem. A* **2007**, *111*, 2951. (f) Ito, A.; Sakamaki, D.; Ino, H.; Taniguchi, A.; Hirao, Y.; Tanaka, K.; Kanemoto, K.; Kato, T. *Eur. J. Org. Chem.* **2009**, 4441.

(10) (a) Lambert, C.; Nöll, G. *Angew. Chem., Int. Ed.* **1998**, *37*, 2107. (b) Lambert, C.; Nöll, G. *Chem.—Eur. J.* **2002**, *8*, 3467.

(11) (a) Stickley, K. R.; Selby, T. D.; Blackstock, S. C. *J. Am. Chem. Soc.* **1994**, *116*, 11576. (b) Stickley, K. R.; Selby, T. D.; Blackstock, S. C. *J. Org. Chem.* **1997**, *62*, 448. (c) Selby, T. D.; Blackstock, S. C. *J. Am. Chem. Soc.* **1998**, *120*, 12155. (d) Selby, T. D.; Kim, K.-Y.; Blackstock, S. C. *Chem. Mater.* **2004**, *14*, 1685. (e) Kim, K.-Y.; Hassenzähl, J. D.; Selby, T. D.; Szulczewski, G. J.; Blackstock, S. C. *Chem. Mater.* **2004**, *14*, 1691. (f) Li, J. C.; Kim, K.-Y.; Blackstock, S. C.; Szulczewski, G. J. *Chem. Mater.* **2004**, *16*, 4711. (j) Li, J. C.; Blackstock, S. C.; Szulczewski, G. J. *J. Phys. Chem. B* **2006**, *110*, 17493. (h) Chotsuwan, C.; Blackstock, S. C. *J. Am. Chem. Soc.* **2008**, *130*, 12556.

(12) Wienk, M. M.; Janssen, R. A. J. *J. Am. Chem. Soc.* **1997**, *119*, 4492.

Chart 1. Dendritic Oligoarylamines **1** and **2**

extensively studied, we revisited to elucidate the spin electronic structure of the charged species in more detail. To enhance both the electron-donating property and the stability of the generated charged species, the dendritic oligotriarylamines **1** and **2** contain the methoxy groups at all the *para*-positions of the peripheral phenyl rings. Herein, we report the synthesis and electrochemical properties of **1** and **2**, and in particular, the electronic structures including intramolecular spin distribution in the charged states for **1** and **2**, based on the absorption and ESR spectroscopic studies.

### Experimental Details

**Synthesis and Characterization.** Commercial-grade reagents were used without further purification. Solvents were purified, dried, and degassed following standard procedures. The synthesis of triamine (**3**) was performed according to a previously reported procedure for the unsubstituted triamine.<sup>9c</sup> Column chromatography was performed using silica gel (Kanto Chemical Co., Inc., Silica gel 60N, spherical neutral). <sup>1</sup>H and <sup>13</sup>C spectra were recorded on a JEOL JNM-AL400 FT NMR spectrometer and chemical shifts are given in parts per million (ppm) relative to internal tetramethylsilane ( $\delta$  0.00 ppm). Elemental analyses were performed by Center for Organic Elemental Microanalysis, Kyoto University.

**Dendritic Oligoarylamine 1.** Triamine **3** (0.62 g, 0.99 mmol), 1,4-dibromobenzene (0.078 g, 0.33 mmol), Pd(OAc)<sub>2</sub> (0.0046 g, 0.020 mmol), DPPF (0.0022 g, 0.040 mmol), and NaOt-Bu (0.11 g, 1.2 mmol) was charged into a clean dry flask under an argon atmosphere, and then anhydrous toluene (20 mL) was added. The resulting solution was refluxed under an argon atmosphere for 4 days. The reaction mixture was washed with aqueous solution of NaHCO<sub>3</sub>, and then the organic layer was dried over Na<sub>2</sub>SO<sub>4</sub>. After evaporation of the solvent, column chromatography on silica gel with toluene afforded **1** (0.33 g, 76.2%) as a yellow powder. <sup>1</sup>H NMR (400 MHz, THF-*d*<sub>8</sub>)  $\delta$  (ppm) 6.97 (m, 18H), 6.88 (m, 12H), 6.79 (m, 24H), 3.72 (s, 24H). <sup>13</sup>C NMR (100 MHz, C<sub>6</sub>D<sub>6</sub>)  $\delta$  (ppm) 156.0, 144.3, 143.2, 142.3, 142.0, 126.2, 125.3,

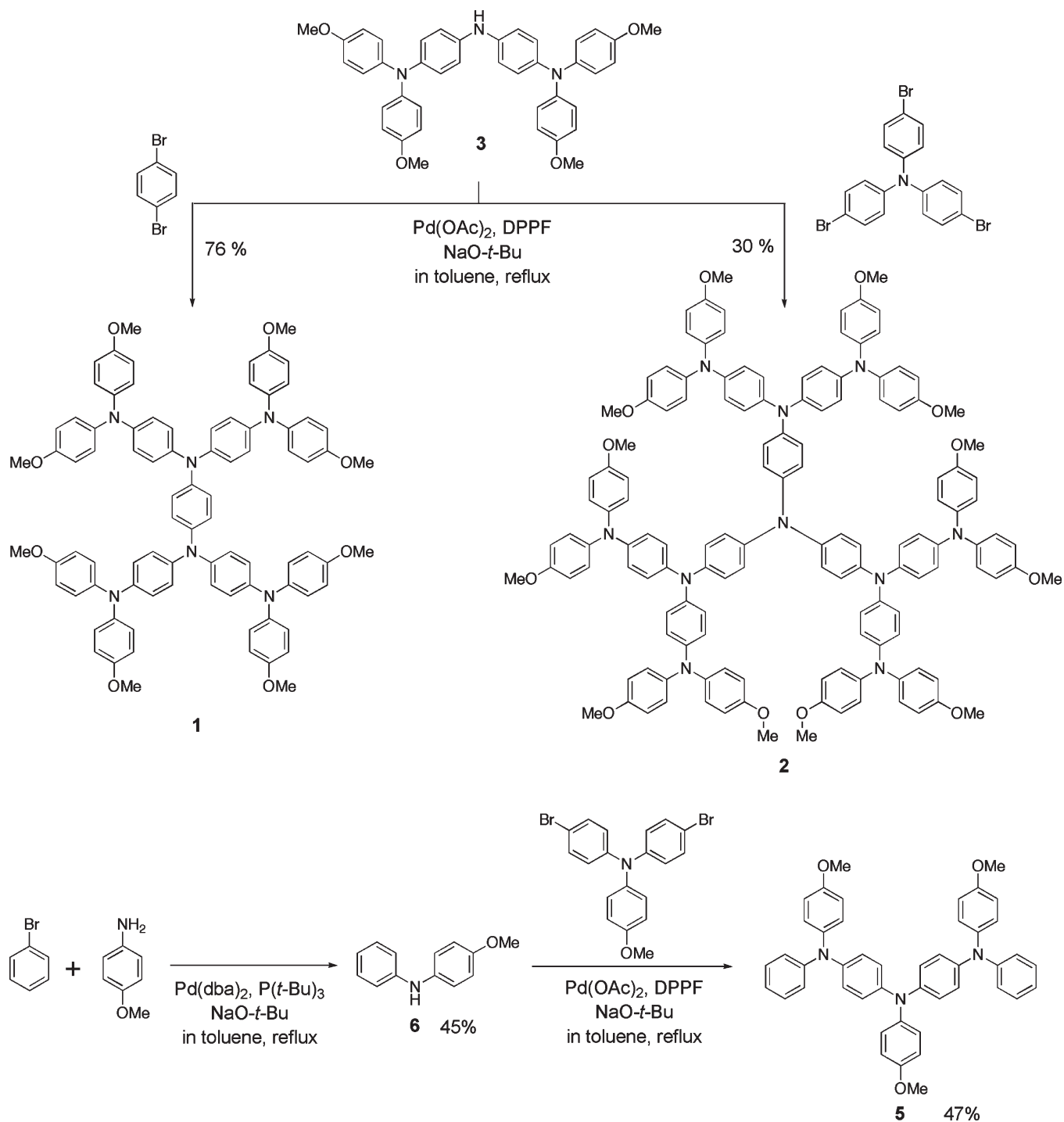
124.7, 123.3, 115.1, 55.1. MS (FABMS): calculated [M-H<sup>+</sup>] for C<sub>86</sub>H<sub>77</sub>N<sub>6</sub>O<sub>8</sub>,  $m/z$  = 1321.5590; found  $m/z$  = 1321.5803. Anal. Calcd for C<sub>86</sub>H<sub>76</sub>N<sub>6</sub>O<sub>8</sub>: C, 78.16; H, 5.80; N, 6.36; O, 9.69. Found: C, 78.35; H, 6.11; N, 6.06; O, 9.94.

**Dendritic Oligoarylamine 2.** Triamine **3** (1.25 g, 2.0 mmol), tris-(4-bromophenyl)amine (0.24 g, 0.50 mmol), Pd(OAc)<sub>2</sub> (0.0067 g, 0.030 mmol), DPPF (0.0033 g, 0.060 mmol) and NaOt-Bu (0.17 g, 1.8 mmol) was charged into a clean dry flask under an argon atmosphere, and then anhydrous toluene (20 mL) was added. The resulting solution was refluxed under an argon atmosphere for 4 days. The reaction mixture was washed with aqueous solution of NaHCO<sub>3</sub>, and the organic layer was then dried over Na<sub>2</sub>SO<sub>4</sub>. After evaporation of the solvent, column chromatography on silica gel with toluene afforded **2** (0.32 g, 30.3%) as a greenish powder. <sup>1</sup>H NMR (400 MHz, THF-*d*<sub>8</sub>)  $\delta$  (ppm) 6.96 (m, 24H), 6.89 (m, 24H), 6.79 (m, 36H), 3.72 (s, 36H). <sup>13</sup>C NMR (100 MHz, THF-*d*<sub>8</sub>)  $\delta$  (ppm) 155.8, 143.9, 141.4, 141.3, 125.7, 125.6, 124.8, 124.6, 124.2, 123.4, 122.2, 114.4, 54.7. Anal. Calcd for C<sub>138</sub>H<sub>120</sub>N<sub>10</sub>O<sub>12</sub>: C, 78.54; H, 5.73; N, 6.64; O, 9.10. Found: C, 77.83; H, 5.73; N, 6.45; O, 8.96.

**4-Methoxydiphenylamine 6.** A mixture of bromobenzene (0.250 g, 2.03 mmol), *p*-anisidine (0.314 g, 2.00 mmol), Pd(dba)<sub>2</sub> (0.057 g, 0.10 mmol), P(*t*-Bu)<sub>3</sub> (0.040 g, 0.20 mmol), and NaOt-Bu (0.311 g, 3.24 mmol) in toluene (22 mL) was refluxed under an argon atmosphere for 23 h. The resulting mixture was washed with brine, and then the organic layer was dried over MgSO<sub>4</sub>. After evaporation of the solvent, the crude product was chromatographed on silica gel with toluene as eluent to afford **6** (0.180 g, 45%) as faint yellow powder. <sup>1</sup>H NMR (400 MHz, acetone-*d*<sub>6</sub>)  $\delta$  (ppm) 7.16 (m, 2H), 7.09 (d, 2H,  $J$  = 9.0 Hz), 7.04 (br s, 1H), 6.95 (m, 2H), 6.87 (d, 2H,  $J$  = 9.0 Hz), 6.73 (t, 1H,  $J$  = 7.3 Hz), 3.76 (s, 3H). <sup>13</sup>C NMR (100 MHz, C<sub>6</sub>D<sub>6</sub>)  $\delta$  (ppm) 145.72, 136.10, 129.51, 128.56, 122.62, 119.71, 115.99, 114.93, 55.13.

**4-Methoxy-4',4''-bis[*N*-(4-methoxyphenyl)-*N*-phenylamino]-triphenylamine 5.** A mixture of **6** (0.166 g, 0.83 mmol), 4-methoxy-*N,N*-bis(4-bromophenyl)aniline (0.132 g, 0.30 mmol), Pd(OAc)<sub>2</sub> (0.009 g, 0.04 mmol), 1,1'-bis(diphenylphosphanyl)ferrocene (0.047 g, 0.08 mmol), and NaOt-Bu (0.119 g, 1.24 mmol) in toluene (8 mL) was refluxed under an argon atmosphere

Scheme 1. Syntheses of 1, 2, and 5



for 19 h. The resulting mixture was washed with brine, and then the organic layer was dried over MgSO<sub>4</sub>. After evaporation of the solvent, the crude product was chromatographed on silica gel with toluene as eluent to afford **5** (0.096 g, 47%) as white powder. <sup>1</sup>H NMR (400 MHz, acetone-*d*<sub>6</sub>) δ (ppm) 7.20 (dd, 4H, *J* = 8.8, 7.3 Hz), 7.08 (d, 2H, *J* = 9.0 Hz), 7.05 (d, 4H, *J* = 9.0 Hz), 6.92 (m, 20H), 3.79 (s, 6H), 3.78 (s, 3H). <sup>13</sup>C NMR (100 MHz, C<sub>6</sub>D<sub>6</sub>) δ (ppm) 156.59, 156.49, 152.03, 149.06, 143.72, 142.87, 141.33, 129.39, 128.57, 127.40, 127.12, 125.24, 124.21, 122.32, 121.52, 115.20, 55.05, 55.05.

**Theoretical Calculations.** Quantum chemical calculations were carried out using a hybrid Hartree–Fock/density functional theory (HF/DFT) method (B3LYP).<sup>13</sup> Full geometrical optimization of **1**, **2**, **5**, and their radical cations were conducted under *D*<sub>2</sub>, *D*<sub>3</sub> and *C*<sub>1</sub> symmetrical constraints for **1**, **2**, and **5** respectively. Excitation energies for the radical cations of **1**, **2**, and **5** were examined on the basis of the time-dependent density functional method (TD–DFT).<sup>14</sup> All the computations employed

(13) Ragavachari, K. *Theor. Chem. Acc.* **2000**, *103*, 361 and references cited therein.

(14) (a) Bauernschmitt, R.; Ahlrichs, R. *Chem. Phys. Lett.* **1996**, *256*, 454. (b) Casida, M. E.; Jamorski, C.; Casida, K. C.; Salahub, D. R. *J. Chem. Phys.* **1998**, *108*, 4439. (c) Stratmann, R. E.; Scuseria, G. E.; Frisch, M. J. *J. Chem. Phys.* **1998**, *109*, 8218.

the 3-21G basis set.<sup>15</sup> All these quantum chemical approaches are implemented in Gaussian 03 package of ab initio MO calculation.<sup>16</sup>

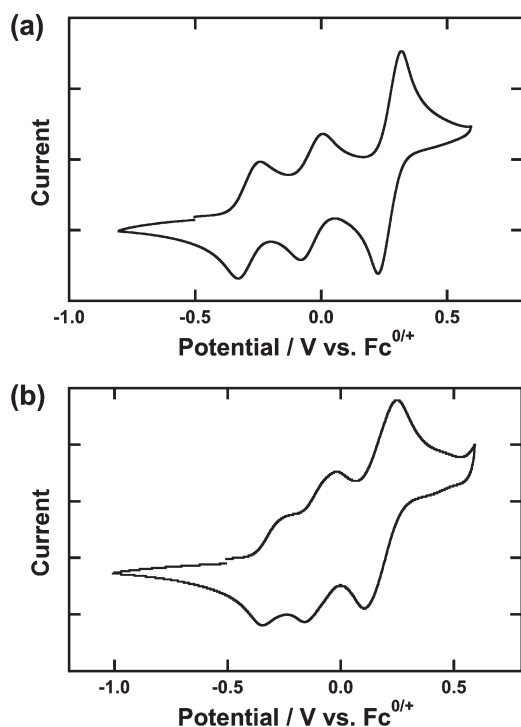


**Figure 1.** Cyclic voltammograms of (a) **1** and (b) **2**, in CH<sub>2</sub>Cl<sub>2</sub>/0.1 M *n*-Bu<sub>4</sub>NBF<sub>4</sub> at 298 K (scan rate 100 mV s<sup>-1</sup>).

**Table 1.** Redox Potentials (*V* vs Fc<sup>0/+</sup>) and Potential Differences of **1–5** and TAPD in CH<sub>2</sub>Cl<sub>2</sub> at 298 K

	<i>E</i> <sub>1</sub>	<i>E</i> <sub>2</sub>	<i>E</i> <sub>3</sub>	<i>E</i> <sub>4</sub>	<i>E</i> <sub>5</sub>	<i>E</i> <sub>6</sub>	Δ <i>E</i> <sub>1–2</sub>
<b>1</b> <sup>a</sup>	−0.28	−0.03	+0.28 <sup>b</sup>	0.79	0.96		0.25
<b>2</b> <sup>a</sup>	−0.30	−0.12	−0.06	0.18 <sup>c</sup>	0.76	0.99	0.18
<b>3</b> <sup>a</sup>	−0.19	+0.11	+0.71 <sup>d</sup>	0.90			0.30
<b>4</b> <sup>e</sup>	−0.16	+0.17	+0.56				0.33
<b>5</b> <sup>e</sup>	−0.11	+0.25	+0.83 <sup>d</sup>				0.36
TAPD <sup>f</sup>	−0.13	+0.35					0.48

<sup>a</sup>Reversible oxidation potentials were digitally simulated. <sup>b</sup>Quasi-two-electron oxidation. <sup>c</sup>Quasi-three-electron oxidation. <sup>d</sup>Oxidation peak potential (irreversible). <sup>e</sup>See ref 11f. The reported oxidation potentials vs SCE were corrected by the redox potential of Fc<sup>0/+</sup> vs SCE (+0.48 V in CH<sub>2</sub>Cl<sub>2</sub>).<sup>19,f</sup>See ref 18.

### Electrochemical and Spectroelectrochemical Measurements.

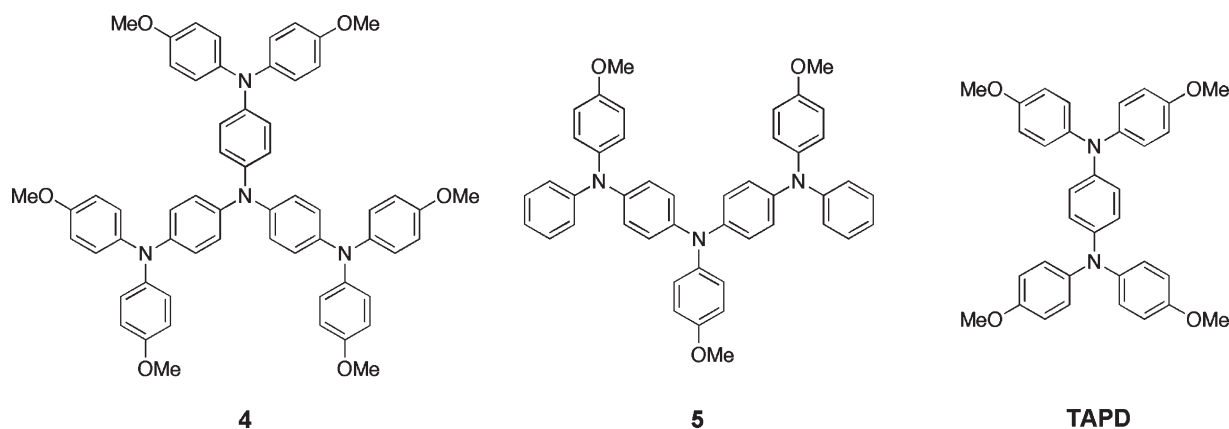
Cyclic voltammograms were recorded using an ALS/chi electrochemical analyzer model 612A with a three-electrode cell using a Pt disk (2 mm<sup>2</sup>) as the working electrode, a Pt wire as the counter electrode, and an Ag/0.01 M AgNO<sub>3</sub> (MeCN) as the reference electrode calibrated against a ferrocene/ferrocenium (Fc<sup>0/+</sup>) redox couple in a solution of 0.1 M tetra-*n*-butylammonium tetrafluoroborate as a supporting electrolyte (298 K, scan rate 100 mV s<sup>-1</sup>). The absorption spectra were measured with a Perkin–Elmer Lambda 19 spectrometer. Spectroelectrochemical measurements were carried out with a custom-made optically transparent thin-layer electrochemical (OTTLE) cell (light pass length = 1 mm) equipped with a platinum mesh, a platinum coil, and a silver wire as the working, the counter, and the pseudoreference electrodes, respectively. The potential was applied with an ALS/chi electrochemical analyzer model 612A.

**ESR Measurements.** ESR spectra were measured using a JEOL JES-TE200 X-band spectrometer in which temperatures were controlled by a JEOL ES-DVT3 variable-temperature unit.

## Results and Discussion

**Synthesis and Electrochemical Studies.** The syntheses of the dendritic oligoarylamines **1** and **2** were carried out in 76 and 30% yield, respectively, by using a palladium-catalyzed Buchwald–Hartwig amination reaction between triamine **3** and the corresponding benzene halides (Scheme 1).<sup>17</sup> The redox properties of **1** and **2** were evaluated by cyclic voltammetry (CV) in CH<sub>2</sub>Cl<sub>2</sub> solution at 298 K with 0.1 M tetra-*n*-butylammonium tetrafluoroborate as supporting electrolyte. Both **1** and **2** exhibited five redox couples as shown in Figure S1 in the Supporting Information. However, the first three reversible oxidation processes are chemically stable after repeated potential cycling in CH<sub>2</sub>Cl<sub>2</sub> (Figure 1). The oxidation potentials [*E*<sub>ox</sub> vs Fc<sup>0/+</sup> (*ne*)] of **1** were determined to be −0.28 (1e), −0.03 (1e), and +0.28 (2e) by digital simulations (see Figure S2a in the Supporting Information), and therefore, **1** is stably oxidizable up to tetracation. The first and third oxidation potentials [*E*<sub>ox</sub> vs Fc<sup>0/+</sup> (*ne*)] of **2** were determined to be −0.30 (1e) and +0.18 (3e), and the second oxidation process was demonstrated to be two separate one-electron-oxidation processes [−0.12 (1e) and −0.06 (1e)] by digital simulations (see Figure S2b in the Supporting Information). Hence, **2** is stably oxidizable up to hexacation. The lower

**Chart 2.** Related Compounds **4**, **5**, and TAPD



first oxidation potentials of **1** and **2** indicate that the present dendritic oligoarylamines are promising as hole transport materials because of strong electron-donating properties. The results are summarized in Table 1, together with those of the related compounds [**3**, **4**,<sup>11f</sup> **5**, *N,N,N',N'*-tetraanisyl-1,4-benzenediamine (**TAPD**)<sup>18</sup> (Chart 2)] under the same conditions. It should be noted that the potential differences between first and second oxidation potentials ( $\Delta E_{1-2}$ ) of **1** and **2** are smaller than that of **TAPD**, in which the radical cation is stabilized by charge delocalization via  $\pi$ -conjugation. This strongly suggests that planarity (or  $\pi$ -conjugation) of **1** and **2** decreases to some extent as compared to that of **TAPD**, because of hyperbranched structures in **1** and **2**.

**Spectroelectrochemical Studies.** To investigate the charge distribution in the charged states of **1** and **2**, we measured the optical absorption spectral changes of **1** and **2** in  $\text{CH}_2\text{Cl}_2$  during the course of the oxidation going from neutral to  $\text{I}^{4+}$

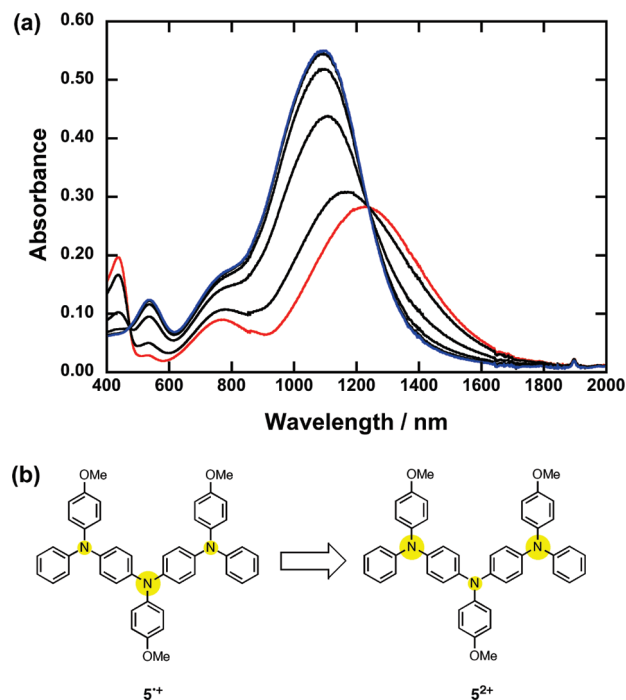


**Figure 2.** (a) UV/vis/NIR spectra of the stepwise electrochemical oxidation of  $5^{2+}$  (in red) to  $5^{2+}$  (in blue) in  $\text{CH}_2\text{Cl}_2/0.1 \text{ M } n\text{-Bu}_4\text{NBF}_4$  at room temperature. It was confirmed by global analysis with HypSpec<sup>20</sup> that no other species than  $5^{2+}$  and  $5^{2+}$  contain in this spectral change. (b) Schematic Mulliken charge distributions (in yellow) of  $5^{2+}$  and  $5^{2+}$  at the B3LYP/3-21G calculations.

or  $2^{6+}$  by using an optically transparent thin-layer electrochemical cell. First of all, we started to check the spectral change from  $5^{2+}$  to  $5^{2+}$ , because **5** can be considered to be a good reference compound for the dendron groups in **1** and **2**. Moreover, the previous studies have already established that the radical cation of the unsubstituted compound of **5** is in a charge resonance (CR) intervalence (IV) state.<sup>9c</sup> It should be noted that the CR states in IV compounds containing three redox-active centers like **5** differ from those in IV compounds with two redox-active centers. CR IV compounds with multiple redox-centers have inevitably unsymmetrical charge distribution, originating from the

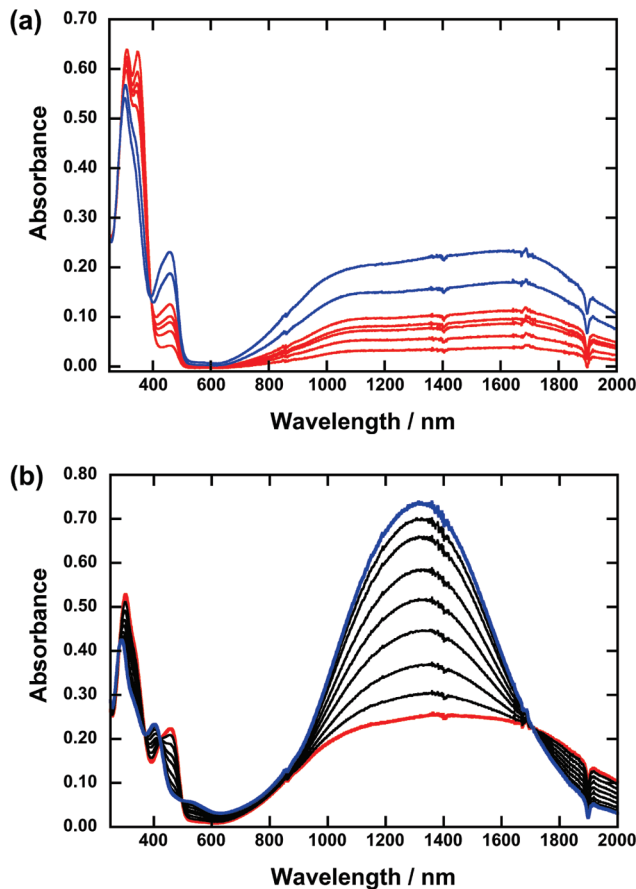


**Figure 3.** UV/vis/NIR spectra of the stepwise electrochemical oxidation of (a) **1** to  $1^{2+}$  (in red) and  $1^{2+}$  to  $1^{2+}$  (in blue) and (b)  $1^{2+}$  (in red) to  $1^{4+}$  (in blue) in  $\text{CH}_2\text{Cl}_2/0.1 \text{ M } n\text{-Bu}_4\text{NBF}_4$  at room temperature. It was confirmed by the global analysis with HypSpec<sup>20</sup> that no other species than **1**,  $1^{2+}$ , and  $1^{4+}$  contain in these spectral changes.

**Table 2.** TD-DFT (UB3LYP/3-21G) Calculations of the Low-Energy Excitation Energies for  $1^{2+}$ ,  $2^{2+}$ ,  $5^{2+}$ , and  $5^{2+}$

species	$h\nu$ (obs) (eV)	$h\nu$ (eV) (f)	TD-DFT calcn	
				assignment
$1^{2+}$	0.75	0.52 (0.52)	348 $\beta$ (HOMO) $\rightarrow$ 349 $\beta$ (LUMO)	
	1.18	0.90 (0.36)	347 $\beta$ ((HO-1)MO) $\rightarrow$ 349 $\beta$ (LUMO)	
		0.92 (0.16)	346 $\beta$ ((HO-2)MO) $\rightarrow$ 349 $\beta$ (LUMO)	
$2^{2+}$	0.67	0.50 (0.41)	555 $\beta$ , 556 $\beta$ (HOMOs) $\rightarrow$ 557 $\beta$ (LUMO)	
	0.99	0.86 (0.28)	554 $\beta$ ((HO-1)MO) $\rightarrow$ 557 $\beta$ (LUMO)	
$5^{2+}$	0.99	0.94 (0.49)	176 $\beta$ (HOMO) $\rightarrow$ 177 $\beta$ (LUMO)	
	1.62	1.38 (0.18)	175 $\beta$ ((HO-1)MO) $\rightarrow$ 177 $\beta$ (LUMO)	
$5^{2+}$	1.13	1.16 (0.99)	176 (HOMOs) $\rightarrow$ 177 (LUMO)	
	$\sim 1.65$ (sh)	1.52 (0.44)	175 ((HO-1)MO) $\rightarrow$ 177 (LUMO)	
	2.34	2.03 (0.18)	173 ((HO-3)MO) $\rightarrow$ 177 (LUMO)	

unsymmetrical molecular structures, whereas CR IV compounds with two redox-active centers have usually symmetrical charge distribution. Note that the electronic structure for the CR IV compounds can be explained by the quantum chemical calculations such as MO and/or DFT calculations. As shown in Figure 2, the lowest energy bands at 0.99 eV (1250 nm) in  $5^{+}$  was changed into more intense band at 1.13 eV (1100 nm) in  $5^{2+}$  with an isosbestic point at 1.01 eV (1225 nm). Judging from the DFT calculations of  $5^{+}$  and  $5^{2+}$ , the charge distribution can be predicted to be completely changed; the generated charge in  $5^{+}$  is distributed mainly on the inner triarylamine moiety, whereas the charge in  $5^{2+}$  is distributed mainly on the outer triarylamine moieties to avoid the electrostatic repulsion between two charges (Figure 2). Herein note that the delocalized electronic state in CR IV compounds with multiple redox-active centers do not necessarily have the symmetrical charge distribution among the redox-active centers. As is the same as the radical cation of the unsubstituted compound of  $5^{+}$ , the lowest energy band of both  $5^{+}$  can be assigned to the transition from  $\beta$  (HOMO) to  $\beta$  (LUMO) on the basis of the time-dependent density functional theory (TD-DFT) calculations. In addition, the TD-DFT calculations showed that the lowest energy band of  $5^{2+}$  is also due to the transition from HOMO to LUMO. The calculated results are summarized in Table 2 together with those for the next lowest band of  $5^{+}$  and  $5^{2+}$ . Note that the difference in relative intensity of the lowest energy band between  $5^{+}$  and  $5^{2+}$  is well-reproduced by the calculated oscillator strengths. The fact that the TD-DFT calculations can explain the observed absorption spectral change strongly suggests that both  $5^{+}$  and  $5^{2+}$  are in the CR IV states: the charge distribution for the CR state of  $5^{2+}$  is determined by the electrostatic repulsion between the charged centers.

In view of change in charge distribution between  $5^{+}$  and  $5^{2+}$ , let us then turn to the spectral change observed during the stepwise electrochemical oxidations of **1** and **2**. During the electrochemical oxidation of **1**, a lowest energy band appeared at 1650 nm (0.75 eV) with a shoulder at 1050 nm (1.18 eV). This lowest energy band for  $1^{+}$  continued to grow up until the oxidation to  $1^{2+}$  has been completed with an isosbestic point at 390 nm (3.18 eV) (Figure 3a). This observation suggests that  $1^{2+}$  dislikes the quinoid structure, which is seen in the dicationic state of TAPD and its derivatives, probably due to the bulky dendron groups. By increasing the electrode potential to the value of the third oxidation process ( $1^{2+}$  to  $1^{4+}$ ), both of the blue shift (1300 nm

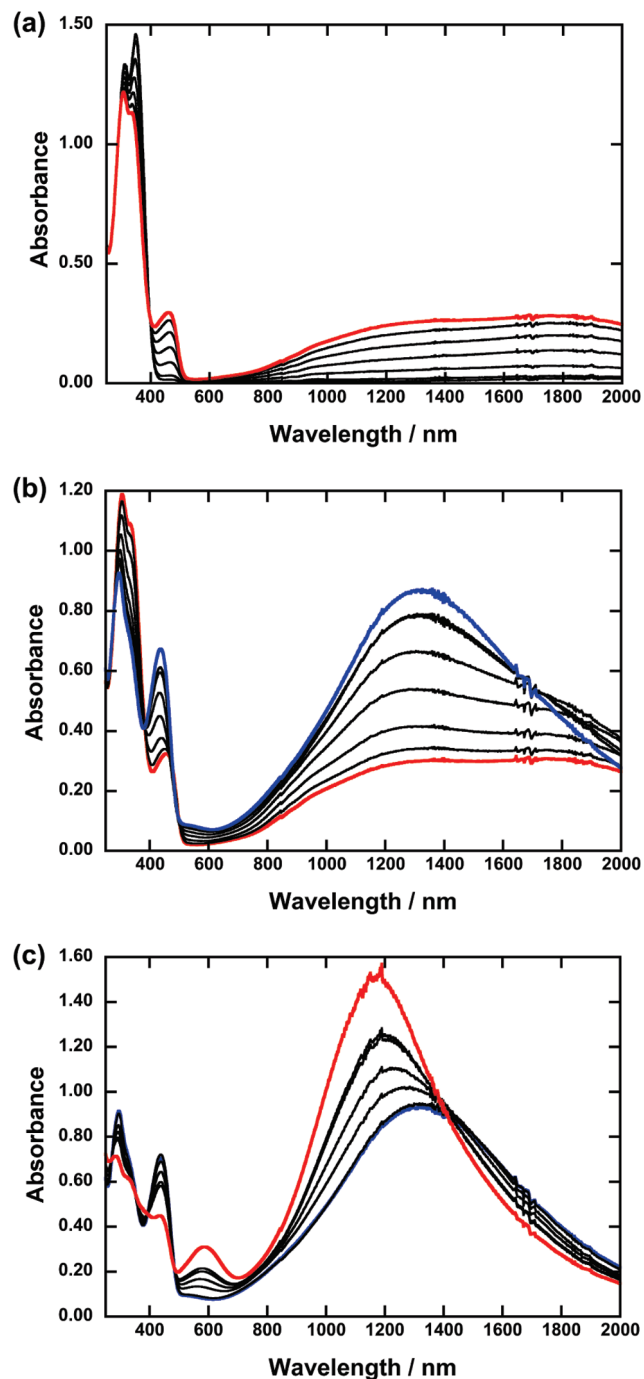


**Figure 4.** UV/vis/NIR spectra of the stepwise electrochemical oxidation of (a) **2** to  $2^{2+}$  (in red), (b)  $2^{2+}$  (in red) to  $2^{3+}$  (in blue), and (c)  $2^{3+}$  (in blue) to  $2^{6+}$  (in red) in  $\text{CH}_2\text{Cl}_2/0.1 \text{ M } n\text{-Bu}_4\text{NBF}_4$  at room temperature. It was confirmed by global analysis with HypSpec<sup>20</sup> that no other species than  $2$ ,  $2^{2+}$ ,  $2^{3+}$ , and  $2^{6+}$  contain in these spectral changes.

(0.95 eV)) and increase in the intensity of the lowest energy band were observed together with several isosbestic points (Figure 3b). This spectral change in the lowest energy band from  $1^{+}$  to  $1^{4+}$  showed the same behavior as that from  $5^{+}$  to  $5^{2+}$ . Hence, it is suggested that the charge distribution changes on going from  $1^{+}$  to  $1^{4+}$ , as shown in Figure 5a.

Similar spectral change was also observed for the electrochemical oxidation of **2**, in which the conjugated  $\pi$ -system is extended by the core triphenylamine and the number of dendron groups. During the electrochemical

- (15) Hehre, W. J.; Radom, L.; Schleyer, P. v. R.; Pople, J. A. *Ab Initio Molecular Orbital Theory*; Wiley: New York, 1986.
- (16) Frisch, M. J.; Trucks, G. W.; Schlegel, H. B.; Scuseria, G. E.; Robb, M. A.; Cheeseman, J. R.; Montgomery, J. A., Jr.; Vreven, T.; Kudin, K. N.; Burant, J. C.; et al. *Gaussian 03*; Gaussian, Inc.: Pittsburgh, PA, 2003.
- (17) (a) Wolfe, J. P.; Wagaw, S.; Buchwald, S. L. *J. Am. Chem. Soc.* **1996**, *118*, 7215. (b) Driver, M. S.; Hartwig, J. F. *J. Am. Chem. Soc.* **1996**, *118*, 7217.
- (18) Ito, A.; Inoue, S.; Hirao, Y.; Furukawa, K.; Kato, T.; Tanaka, K. *Chem. Commun.* **2008**, 3242.
- (19) Kelly, S. L.; Kadish, K. M. *Inorg. Chem.* **1984**, *23*, 679.
- (20) (a) Gans, P.; Sabatini, A.; Vacca, A. *Talanta* **1996**, *43*, 1739. (b) Gans, P.; Sabatini, A.; Vacca, A. *Ann. Chim.* **1999**, *89*, 45.

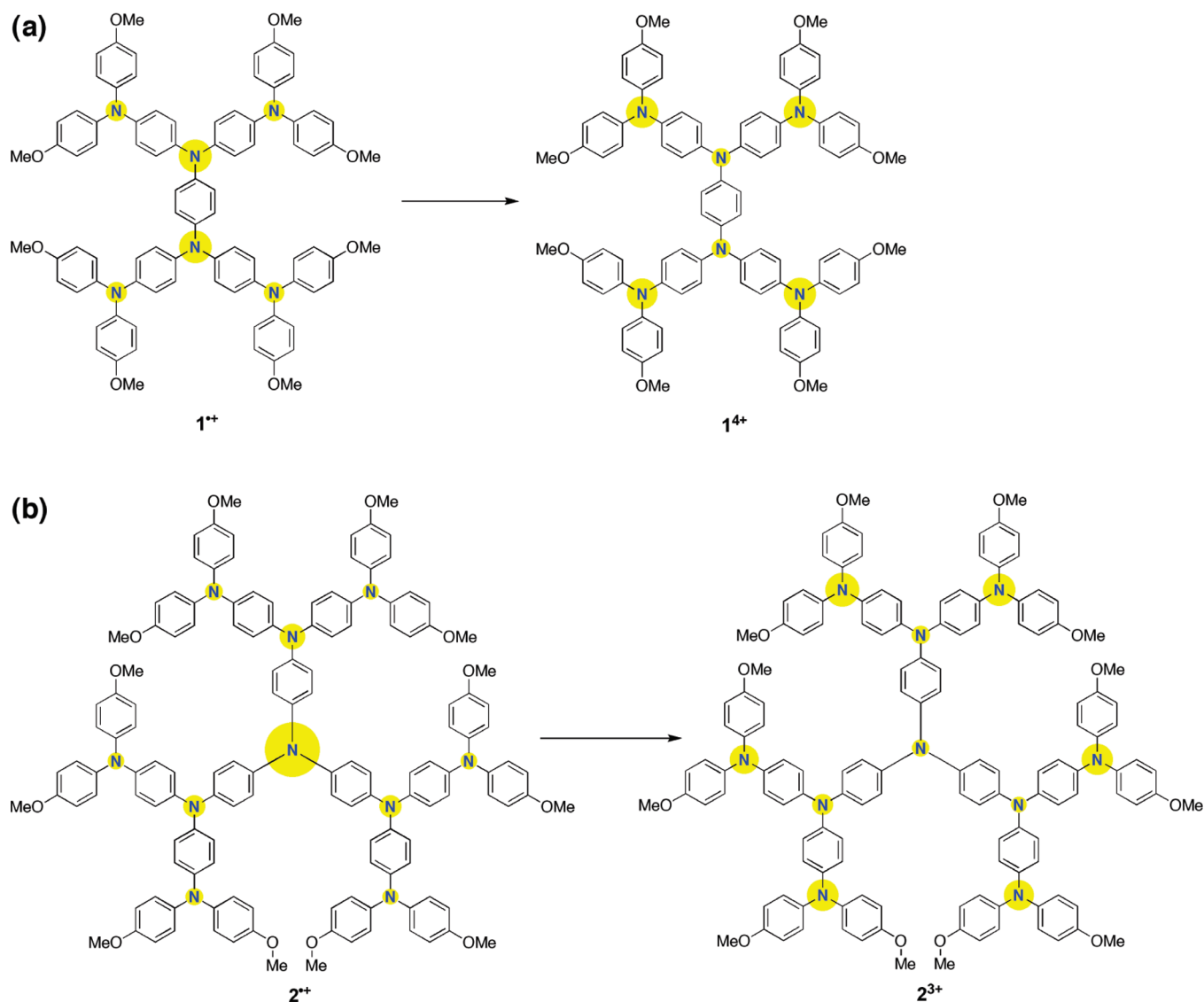


**Figure 5.** Hypothetical charge distributions (in yellow) of (a)  $1^{2+}$  to  $1^{4+}$  and (b)  $2^{2+}$  to  $2^{3+}$ .

oxidation of **2**, a lowest energy band appeared at 1850 nm (0.67 eV) with a shoulder at 1250 nm (0.99 eV) (Figure 4a). By increasing the electrode potential to the value of the second oxidation process ( $2^{2+}$  to  $2^{3+}$ ), both the blue shift (1300 nm (0.95 eV)) and increase in the intensity of the lowest-energy band were observed together with some isosbestic points (Figure 4b). This spectral change in the lowest energy band from  $2^{2+}$  to  $2^{3+}$  showed the same behavior as that from  $5^{2+}$  to  $5^{2+}$ . Hence, it is suggested that the charge distribution changes on going from  $2^{2+}$  to  $2^{3+}$ , as shown in Figure 5b. Moreover, at the electrode potential of the third oxidation process ( $2^{3+}$  to  $2^{6+}$ ), further blue shift (1300 nm (0.95 eV)) and increase in the intensity of the lowest-energy band were observed together with several isosbestic points (Figure 4b). This process corresponds to further charge up on each of the charged dendron groups.

It should be noted that the typical localized triarylamine radical cation bands ( $\sim 750$  nm)<sup>4a,21</sup> are not observed in all the absorption spectra for the charged states of **1**, **2**, and **5**. This strongly suggests that the observed charged states are not in localized IV states but in CR IV states. Furthermore, as will be clarified in the next section, the observed lowest energy bands can be considered as the charge resonance (CR) bands originating from the delocalized electronic states. This means that the usual quantum chemical calculations allow us to assign the lowest energy absorption bands of the charged states of **1** and **2** to specific electronic transitions. Hence, we carried out the TD-DFT calculations<sup>14</sup> on  $1^{2+}$  and  $2^{2+}$ . As is shown in Table 2, it was found that the TD-DFT-calculated results qualitatively elucidated the characteristics of the observed lowest energy bands including relative intensity. The lowest energy band of  $1^{2+}$  can be regarded as an overlap of three transitions: the peak at 0.75 eV can be assigned to the transition from  $\beta$  (HOMO) to  $\beta$  (LUMO), whereas the

(21) (a) Neugebauer, F. A.; Bamberger, S.; Groh, W. R. *Chem. Ber.* **1975**, *108*, 2406. (b) Schmidt, W.; Steckhan, E. *Chem. Ber.* **1980**, *113*, 577. (c) Dapperheld, S.; Steckhan, E.; Grosse Brinkhaus, K.-H.; Ecsch, T. *Chem. Ber.* **1991**, *124*, 2557.

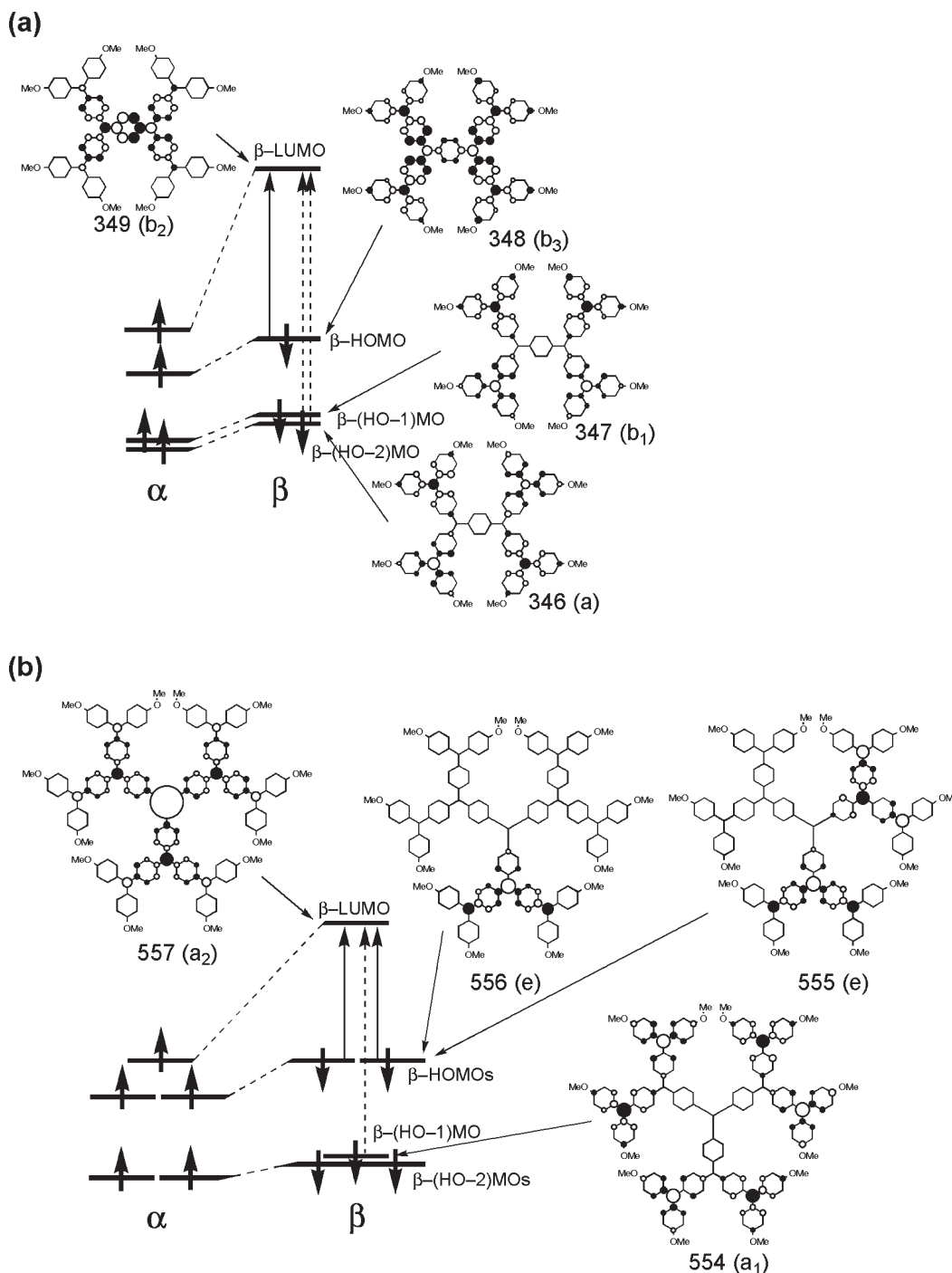


**Figure 6.** Relative energy levels of the frontier MOs for (a)  $1^{1+}$  and (b)  $2^{2+}$  based on the UB3LYP/3-21G calculations. The arrows with solid and dashed lines represent the major contributions to the lowest and next-lowest energy transitions, respectively.

shoulder at 1.18 eV can be assigned to a mixture of two transitions; (i) from  $\beta$  ((HO-1)MO) to  $\beta$  (LUMO), and (ii) from  $\beta$  ((HO-2)MO) to  $\beta$  (LUMO). Similarly, The lowest-energy band of  $2^{2+}$  can be regarded as an overlap of two transitions: the peak at 0.67 eV can be assigned to a transition from doubly degenerate  $\beta$  (HOMOs) to  $\beta$  (LUMO), while the shoulder at 0.99 eV can be assigned to a transition from  $\beta$  ((HO-1)MO) to  $\beta$  (LUMO). As is apparent from the MO energy diagrams in Figure 6, these transitions are explainable to be charge resonance between the peripheral dendron groups and the core amine moieties.

**ESR Studies.** To further evaluate the electronic structure of the charged states of **1** and **2**, the ESR spectra of the chemically oxidized samples in  $\text{CH}_2\text{Cl}_2$  were recorded. In addition, we also checked the ESR spectral change from  $5^{2+}$  to  $5^{1+}$ . The radical cation and dication of **5** were generated by treating with 1 and 2 equiv. of tris(4-bromophenyl)ammonium hexachloroantimonate in  $\text{CH}_2\text{Cl}_2$  at 195 K. As shown in Figure 7a, the ESR spectrum of  $5^{2+}$  showed the similar spectral shape to that of the radical cation for the unsubstituted compound of **5**.<sup>9c</sup> On the basis of the spectrum simulation, the hyperfine coupling constants were determined:  $|a_N| = 0.660$  mT (1N),

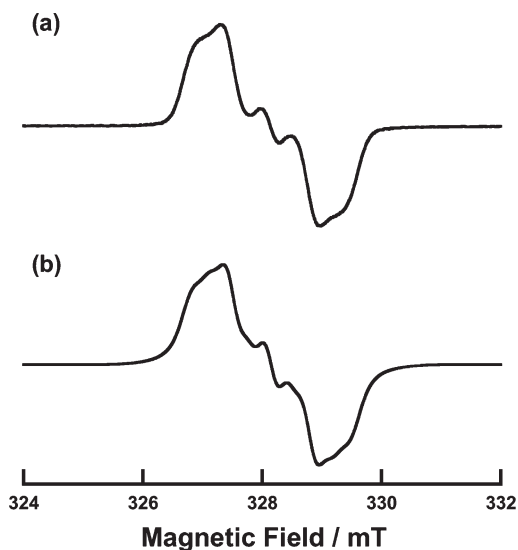


Figure 7. ESR spectrum of  $5^{*+}$ : (a) in  $\text{CH}_2\text{Cl}_2$  at 290 K; (b) simulated.

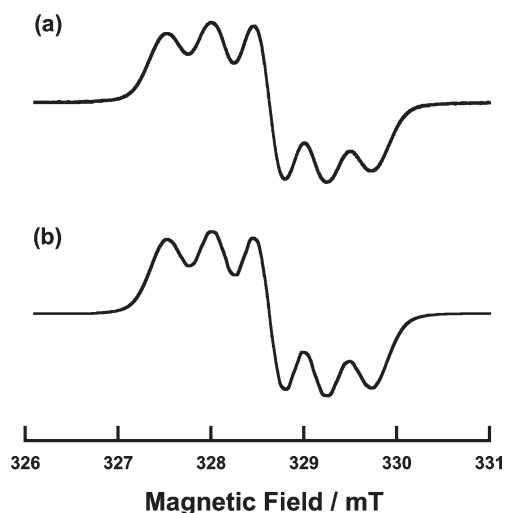


Figure 8. ESR spectrum of  $1^{*+}$ : (a) in  $\text{CH}_2\text{Cl}_2$  at 290 K; (b) simulated.

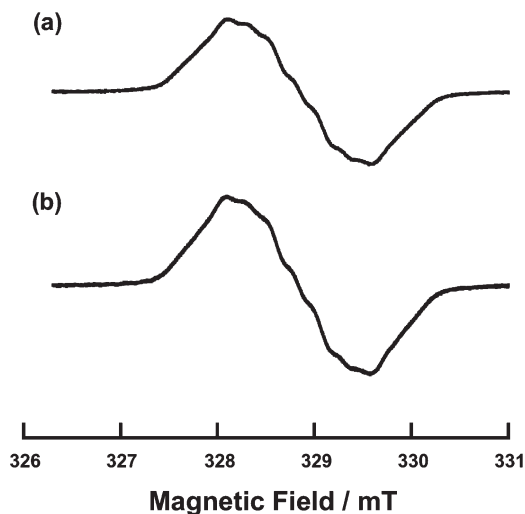


Figure 9. ESR spectrum of  $2^{*+}$ : (a) in  $\text{CH}_2\text{Cl}_2$  at 290 K; (b) simulated.

$|a_{\text{N}}| = 0.275$  mT (2N),  $|a_{\text{H}}| = 0.100$  mT (2H),  $|a_{\text{H}}| = 0.050$  mT (4H),  $|a_{\text{H}}| = 0.030$  mT (8H), and the contributions from

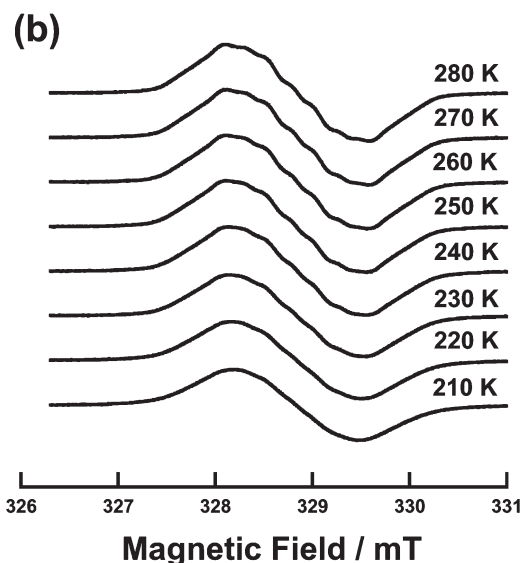
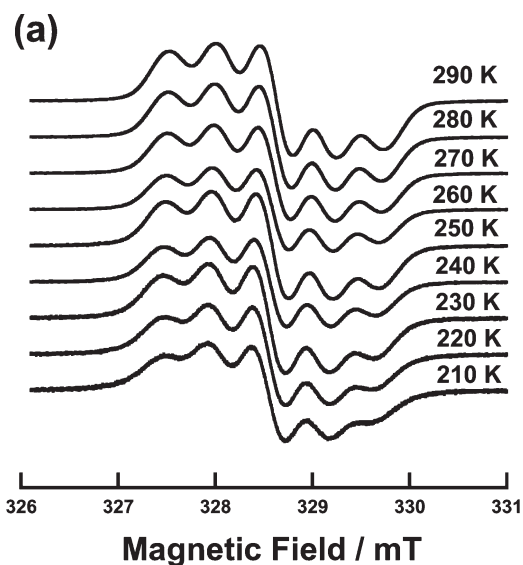
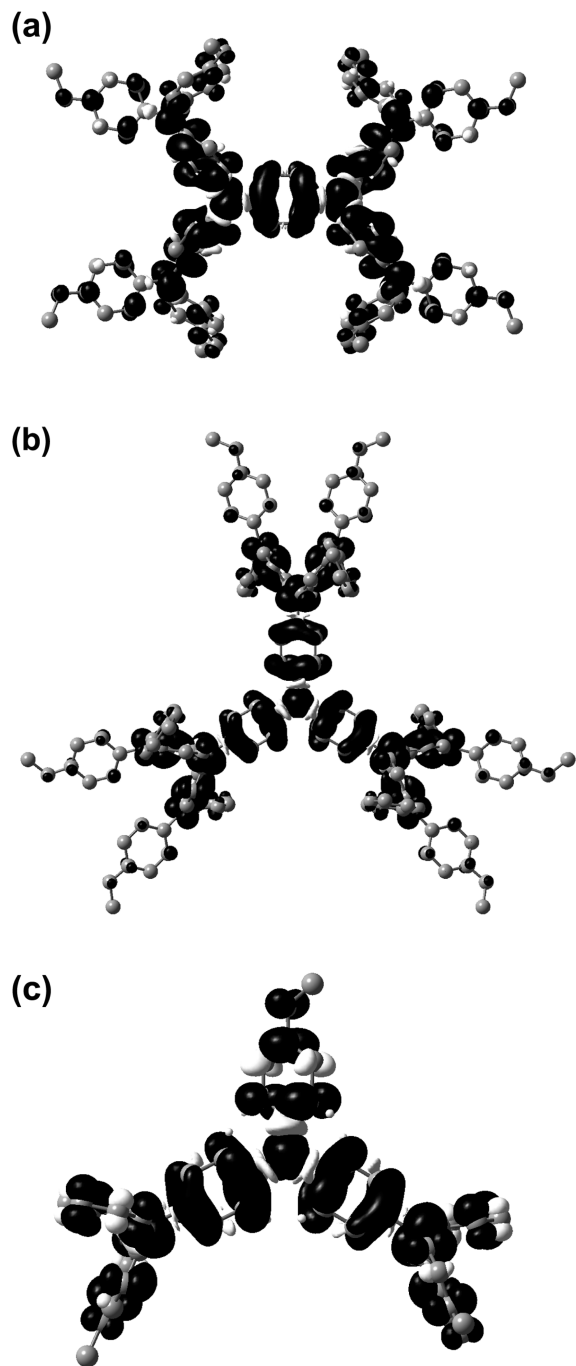


Figure 10. Temperature-dependence of the ESR spectrum for (a)  $1^{*+}$  and (b)  $2^{*+}$  in  $\text{CH}_2\text{Cl}_2$ .

the negligible hydrogen nuclei were incorporated in the line width of the spectral simulation (0.20 mT) (Figure 7b). On the other hand, the dication  $5^{2+}$  was ESR-silent, and therefore, we could not obtain any information on the charge distribution (Figure S4).

The ESR spectra of  $1^{*+}$  and  $2^{*+}$  generated by chemical oxidation of **1** by 1 equiv. of tris(4-bromophenyl)ammonium hexachloroantimonate in  $\text{CH}_2\text{Cl}_2$  at 195 K showed a multiplet hyperfine structures (Figures 8 and 9). Note that  $1^{*+}$  and  $2^{*+}$  were found to be stable under anaerobic conditions at room temperature for a few months, as indicated by there being no loss in the ESR signal intensity. The splitting pattern of  $1^{*+}$  can be explained by the presence of two and four equivalent nitrogen nuclei and 4 equivalent hydrogen nuclei originating from the central *para*-phenylene moiety, although the broadness of the signals suggests additional small hyperfine coupling constants due to the other hydrogen nuclei (Figure 8a). The optimum simulation of the observed spectrum gave



**Figure 11.** DFT-computed spin density distributions (black: positive spin, white: negative spin; spin isosurface value = 0.0003 electron/au,<sup>3</sup> UB3LYP/3-21G) of (a)  $1^{\bullet+}$ , (b)  $2^{\bullet+}$ , and (c)  $5^{\bullet+}$ .

the following hyperfine coupling constants:  $|a_{\text{N}}| = 0.455$  mT (2N),  $|a_{\text{N}}| = 0.100$  mT (4N), and  $|a_{\text{H}}| = 0.060$  mT (4H), and the contributions from the negligible hydrogen nuclei were incorporated in the line width of the spectral simulation (0.10 mT) (Figure 8b). On the other hand, the generated  $1^{2+}$  gave an ESR spectrum with no hyperfine nor fine structures, and therefore, we could not extract any information on the charge distribution from the spectrum (see Figures S5a and S6a in the Supporting Information).

On the one hand, the hyperfine structure of  $2^{\bullet+}$  was clarified by the presence of one, three and six equivalent

nitrogen nuclei and 12 equivalent hydrogen nuclei originating from the central triphenylamine moiety, although the broadness of the signals suggests additional small hyperfine coupling constants due to the other hydrogen nuclei (Figure 9a). The best fit simulated spectrum was obtained by the following hyperfine coupling constants:  $|a_{\text{N}}| = 0.455$  mT (1N),  $|a_{\text{N}}| = 0.218$  mT (3N),  $|a_{\text{N}}| = 0.047$  mT (6N) and  $|a_{\text{H}}| = 0.033$  mT (12H), and the contributions from the negligible hydrogen nuclei were incorporated in the line width of the spectral simulation (0.10 mT) (Figure 9b). Like  $1^{2+}$ , the generated  $2^{2+}$  also gave an ESR spectrum with no hyperfine nor fine structures, and therefore, we could not extract any information on the charge distribution from the spectrum (see Figures S5b and S6b in the Supporting Information).

It is interesting to note that the ESR spectral shape for both  $1^{\bullet+}$  and  $2^{\bullet+}$  did not change in the temperature range from  $-60$  to  $20$  °C (Figure 10), and hence, the observed temperature independency clearly demonstrated that the both  $1^{\bullet+}$  and  $2^{\bullet+}$  are in CR IV states. As a consequence, it was found that the generated spins in  $1^{\bullet+}$ ,  $2^{\bullet+}$ , and  $5^{\bullet+}$  are distributed over the dendritic molecular backbones, judging from the hyperfine coupling constants. These spin distributions are in good accordance with the DFT-calculated spin densities on  $1^{\bullet+}$ ,  $2^{\bullet+}$ , and  $5^{\bullet+}$ , as shown in Figure 11. Again, note that the delocalized electronic state in CR IV compounds with multiple redox-active centers like  $1^{\bullet+}$ ,  $2^{\bullet+}$ , and  $5^{\bullet+}$  do not necessarily have the symmetrical charge distribution among the redox-active centers.

## Conclusion

We have reported the synthesis and electrochemical, spectroelectrochemical, ESR spectroscopic results of two kinds of basic dendritic (or starburst) all-*para*-phenylene-linked oligotriarylamines **1** and **2**, which are generated from *para*-phenylenediamin and triphenylamine as core units, respectively. We have demonstrated that **1** and **2** are oxidizable up to tetra- and hexacations, respectively, and, according to the degree of oxidation, the charge distribution of the charged states of **1** and **2** gradually change so as to reduce the electrostatic repulsion between increased charges. Moreover, spin distribution in the CR state for the radical cations of **1** and **2** was confirmed by the ESR measurements. These findings are of great interest in connection with the intermolecular hole hopping transfer in the solid state of the oligoarylamines utilized in hole-transport layer in OLEDs.<sup>22</sup>

**Acknowledgment.** The present work was supported by a Grant-in-Aid for Scientific Research (B) (20350065) from the Japan Society for the Promotion of Science (JSPS).

**Supporting Information Available:** Additional figures (PDF). This material is available free of charge via the Internet at <http://pubs.acs.org>.

- (22) (a) Borsenberger, P. M.; Pantmeier, L.; Bäessler, H. *J. Chem. Phys.* **1991**, *94*, 5447. (b) Borsenberger, P. M.; Weiss, D. S. *Organic Photoreceptors for Imaging Systems*; Marcel Dekker: New York, 1993. (c) Heun, S.; Borsenberger, P. M. *Chem. Phys.* **1995**, *200*, 245.